


Relating galaxies across different redshift to study galaxy evolution

Kai Wang,^{1,2}  Houjun Mo,³ Cheng Li² and Yangyao Chen^{4,5}

¹Kavli Institute for Astronomy and Astrophysics, Peking University, Beijing 100871, China

²Department of Astronomy, Tsinghua University, Beijing 100084, China

³Department of Astronomy, University of Massachusetts Amherst, MA 01003, USA

⁴Key Laboratory for Research in Galaxies and Cosmology, Department of Astronomy, University of Science and Technology of China, Hefei, Anhui 230026, China

⁵School of Astronomy and Space Science, University of Science and Technology of China, Hefei 230026, China

Last updated 2022 October 25; in original form 2022 October 25

ABSTRACT

We propose a general framework leveraging the galaxy-halo connection to link galaxies observed at different redshift in a statistical way, and use the link to infer the redshift evolution of the galaxy population. Our tests based on hydrodynamic simulations show that our method can accurately recover the stellar mass assembly histories up to $z \sim 3$ for present star-forming and quiescent galaxies down to $10^{10} h^{-1} M_{\odot}$. Applying the method to observational data shows that the stellar mass evolution of the main progenitors of galaxies depends strongly on the properties of descendants, such as stellar mass, halo mass, and star formation states. Galaxies hosted by low-mass groups/halos at the present time have since $z \sim 1.8$ grown their stellar mass ~ 2.5 times as fast as those hosted by massive clusters. This dependence on host halo mass becomes much weaker for descendant galaxies with similar star formation states. Star-forming galaxies grow about 2–4 times faster than their quiescent counterparts since $z \sim 1.8$. Both TNG and EAGLE simulations over-predict the progenitor stellar mass at $z > 1$, particularly for low-mass descendants.

Key words: galaxies: evolution - galaxies: haloes - galaxies: statistics - galaxies: stellar content.

1 INTRODUCTION

One goal in galaxy formation and evolution is to establish a predictive formulation of the assembly histories of galaxies and their dark matter halos so as to understand the evolution of galaxies in their stellar populations and gas components (National Academies of Sciences 2021). One way to do this is to establish connections for galaxies observed at different redshift. Galaxy surveys allow us to study galaxy populations in our Universe at different cosmic times (York et al. 2000; Lilly et al. 2009; Gerke et al. 2007; Driver et al. 2022; Tomczak et al. 2014; Takada et al. 2014; Maiolino et al. 2020). However, galaxies at different redshift are not causally connected (see blue points on the left side of Fig. 1). Mathematically, galaxy surveys only provide us with the time-dependent distribution function of galaxy properties, $f(\mathbf{g} | t)$, where \mathbf{g} is the ‘vector’ representing an array of galaxy properties, such as stellar mass, star formation rate, luminosity, and color. The evolution of individual galaxies is then given by $\mathbf{g}(t)$ as a function of t . Unfortunately, we can not obtain $\mathbf{g}(t)$ for individual galaxies observationally. In practice, the observed galaxy populations at different redshift may be connected in a statistical sense, and we can obtain constraints on $\mathbf{g}(t)$ statistically.

In the framework provided by the current cosmology, galaxies form and grow in the gravitational potential of dark matter halos (White & Rees 1978; Mo et al. 2010). Thus the formation history of a galaxy is expected to be closely related to the assembly history of its host halo.

The assembly of a halo is characterized by its merger tree, which describes how the progenitors merge together to form the descendant halo, as illustrated on the right side of Fig. 1. The formation of the halo population in the current cosmological framework is well understood, and large samples of halo merger trees are now available from semi-analytical models and cosmological simulations of dark matter halos. Clearly, the information provided by halo merger trees should be used as a key component in modeling the assembly of galaxies.

In order to use halo merger trees to follow galaxy assembly, it is necessary to link the observed galaxy populations with the halo population. Three approaches have been used to make the link. The first one is to simulate the evolution of different matter components based on first principles, with a set of empirical, subgrid recipes to model some crucial but unresolved processes (e.g. Vogelsberger et al. 2013; Schaye et al. 2015; Vogelsberger et al. 2020; Nelson et al. 2019). The second approach is to model galaxy evolution processes through a set of parametric functions, with the model parameters constrained using summary statistics obtained from galaxy surveys, such as the distribution functions of galaxies with respect to intrinsic properties (e.g. Li & White 2009; Baldry et al. 2012; Moustakas et al. 2013; Davidzon et al. 2017; Chen et al. 2019) and spatial correlation functions of galaxies (e.g. Li et al. 2006). This approach can be further divided into two sub-categories: semi-analytical models (e.g. White & Frenk 1991; Somerville & Primack 1999; Kang et al. 2005; Croton et al. 2006; De Lucia & Blaizot 2007; Benson 2010; Guo et al. 2011; Henriques et al. 2015) and empirical models (Zheng et al. 2007; White et al. 2007; Conroy & Wechsler 2009; Moster et al. 2010; Yang et al. 2012; Lu et al. 2014; Behroozi et al. 2019;

* Contact e-mail: wkcosmology@gmail.com

† Present address: Kavli Institute for Astronomy and Astrophysics, Peking University, Beijing 100871, China

2 - types of
parametric fns. →

semi-analytic = physically motivated
empirical

Kipper et al. 2021), depending on whether the functions describing galaxy evolution processes are physically or empirically motivated. The third approach is to establish the galaxy-halo connection through some **heuristic assumptions**. For instance, van Dokkum et al. (2010) derived the stellar mass evolution histories for massive galaxies assuming that the stellar mass rank of a galaxy is preserved during the time period in question (Brown et al. 2007; Jaacks et al. 2016; Tal et al. 2014). This assumption is expected to be invalid if galaxy mergers are important during the period of interest, or if the variance in the assembly histories is large for the galaxy population in concern (Leja et al. 2013). Behroozi et al. (2013) refined this method and proposed the use of an evolving cumulative number density based on the sub-halo abundance matching method (see also Mo et al. 1999; Yang et al. 2003; Vale & Ostriker 2004; Conroy et al. 2006; Guo et al. 2010; Behroozi et al. 2010; Li et al. 2013; Contreras et al. 2021). In this method, the evolution in the mass rank of subhalos obtained from N -body simulations is used to mimic that in the stellar mass rank of galaxies (Torrey et al. 2015, 2017; Wellons & Torrey 2017; Hill et al. 2017), and it has been shown that this method is able to recover the stellar mass evolution of the main progenitors of galaxies from $z \gtrsim 3$ to $z \sim 0$ in the EAGLE and Illustris simulations (Clauwens et al. 2016; Torrey et al. 2015). The methods based on the cumulative number density of galaxies have been applied to infer the stellar mass growth of massive galaxies and the evolution of their star formation activities and structures (van Dokkum et al. 2010; Hill et al. 2017). However, as found by Clauwens et al. (2016), the stellar mass evolution depends significantly on the star formation states of descendant galaxies at $z = 0$ in the EAGLE simulation, in the sense that passive descendants have more massive progenitor galaxies, especially for low-mass galaxies, and the cumulative number density method is unable to reproduce the trend.

In this paper, we leverage the established galaxy-halo connection to propose a framework to connect galaxies across cosmic time. **The most basic relation between galaxies and dark matter halos is the central galaxy stellar mass- halo mass relation (SMHM relation)**, which may be described by some parametric forms (Yang et al. 2009; Guo et al. 2010; Behroozi et al. 2010; Yang et al. 2012; Wechsler & Tinker 2018). With more information gathered from observations and numerical simulations, it is also possible to study secondary effects in the galaxy-halo connection, and models making use of galaxy and halo properties in addition to mass have been proposed (e.g. Hearin & Watson 2013; Hearin et al. 2014; Watson et al. 2015; Behroozi et al. 2019). Although a consensus is still to be reached, some promising results have been obtained from such modeling. For instance, relating galaxy color to halo formation time as a secondary constraint on the galaxy-halo connection, Hearin & Watson (2013) were able to reproduce the clustering properties for galaxies and their dependence on galaxy color and star formation activity (see also Watson et al. 2015). These results will be used in our method to improve the connection of galaxies across cosmic time and to alleviate some problems in some earlier models. In particular, we connect galaxies at different redshift chronologically by populating them into subhalo merger trees according to the galaxy-halo connection introduced above. **Our incorporation of halo formation times to model galaxy star formation activities also enables us to follow galaxy assembly histories conditioned on the star formation state of descendant galaxies, thus differentiating between active and passive descendants.**

The paper is organized as follows. In § 2, we introduce our framework. We test our method using hydrodynamic simulations in § 3. We apply our method to observational data in § 4. Finally, we summarize our results in § 5.

2 METHOD TO LINK GALAXIES WITH THEIR PROGENITORS

2.1 The framework of connecting galaxies across cosmic time

Here we propose a general framework to connect galaxies across cosmic time. In Fig. 1, the left side shows observed galaxies at different redshift, from which we can calculate the distribution of galaxy properties as a function of redshift. **The right side shows subhalo merger trees constructed from N -body simulations or with semi-analytical methods, where each subhalo can have multiple progenitors but only one descendant.** These connections form the so-called subhalo merger trees. In the current scenario of galaxy formation, galaxies form and evolve in dark matter halos/subhalos. It is thus possible to incorporate the properties of subhalo merger trees when linking galaxies at different cosmic times. This can be done as follows. First, **we use the relation between the subhalo and galaxy populations at a given redshift to link galaxies to subhalos at that redshift**, as indicated schematically by the horizontal lines in Fig. 1. Second, **we use subhalo merger trees to connect galaxies at different redshift according to the subhalos that the galaxies are linked to.** Finally, **we infer the evolution of galaxies based on the link established for galaxies at different redshift.**

The key piece of this method is the relation between subhalos and galaxy populations, and this is the main difference between our work and previous studies (van Dokkum et al. 2010; Behroozi et al. 2013). Behroozi et al. (2013) used the SMHM relation to connect galaxies of a given stellar mass rank to subhalos of the same subhalo mass rank, and to study the stellar mass assembly histories of galaxies. **Here we take a step further by adding the star formation states of galaxies at $z \sim 0$ into the galaxy-subhalo connection. We can thus study the stellar mass assembly histories conditioned on the star formation activities of descendant galaxies.** In addition, we highlight the dependence on the host halo mass of descendant galaxies, which was ignored in previous studies.

2.2 Assigning stellar mass to subhalos

One important part of the framework described above is to link galaxies to dark matter halos at a given redshift. The exact link depends on the details of galaxy formation and evolution in dark matter halos. For an empirical model such as the one considered here, the assumptions adopted in establishing this link need to be sufficiently flexible to allow uncertainties in this link. **We adopt an abundance matching method to link galaxies to subhalos.** In this subsection, we describe our method to link the stellar mass of galaxies to the mass of subhalos, taking into account the scatter in their relation. In the following subsection (§ 2.3), we describe how to assign star formation states to subhalos.

Sub-halo abundance matching (SHAM) is an empirical method to populate galaxies into subhalos, assuming a monotonic relation between one of the galaxy properties (e.g. luminosity and stellar mass) and one of the subhalo properties (e.g. peak halo mass and peak circular velocity) (Mo et al. 1999; Yang et al. 2003; Vale & Ostriker 2004; Conroy et al. 2006; Guo et al. 2010; Behroozi et al. 2010; Li et al. 2013; Contreras et al. 2021). Here we use the stellar mass of galaxies, M_* , and the peak halo mass of subhalos¹, M_p , to perform the SHAM procedure. As found in previous studies, it is important to take into account the variance in the relation between galaxy and

¹ The peak halo mass of a subhalo is defined as the maximum halo mass that a subhalo has achieved along its main branch when it is a central subhalo.

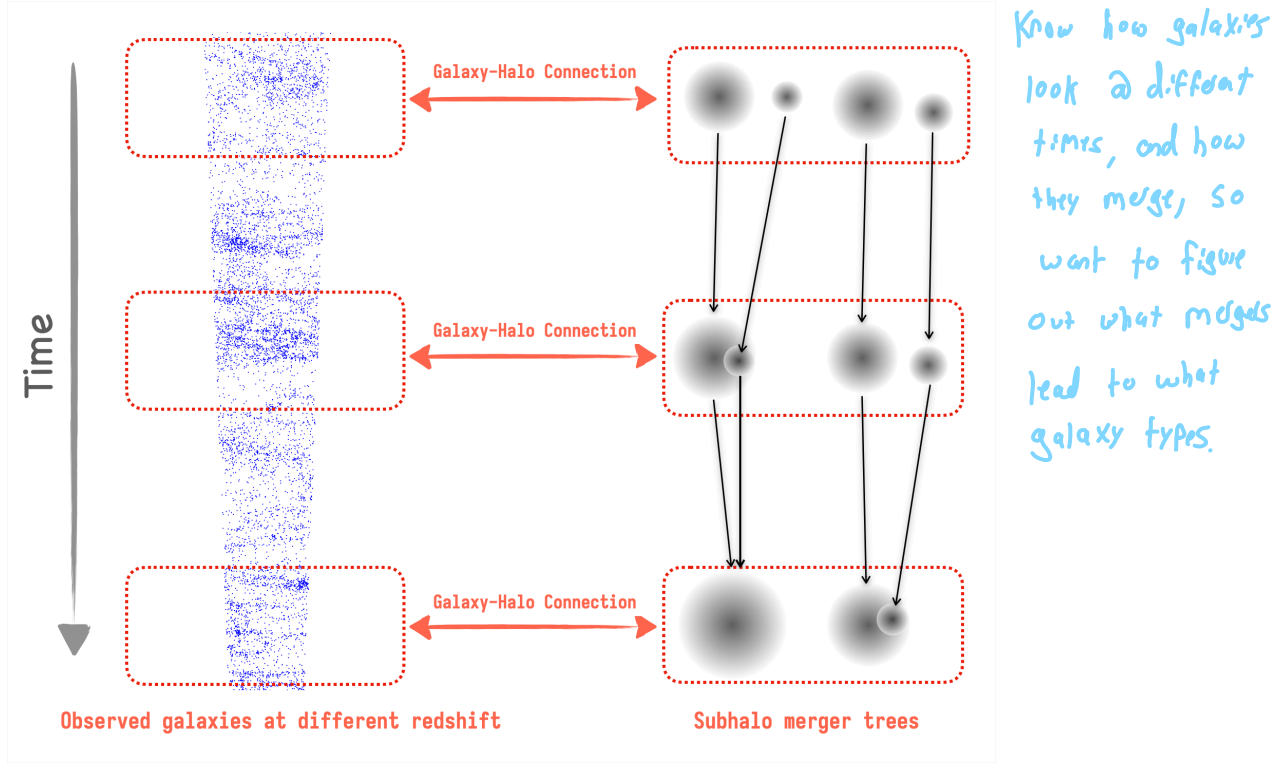


Figure 1. Demonstration of the method that connects galaxies across cosmic time. On the left hand, blue points are the observed galaxies from high redshift (top) to low redshift (bottom). On the right hand, black shades are halos and subhalos on subhalo merger trees from N-body simulations. We first connect galaxies with halos using established galaxy-halo connections, then use links in subhalo merger trees to connect galaxies across cosmic time.

halo properties in order to better reproduce summary statistics of the observed galaxy population, such as the two-point correlation function (Behroozi et al. 2010; Reddick et al. 2013; Hearin et al. 2013). Our model includes such variances. The method consists of the following steps:

- (i) Perform the SHAM procedure for galaxies at $z = 0$ using

$$n(> M_{*,0}) = n(> M_{p,0}), \quad (1)$$

where the left-hand side is the cumulative stellar mass function of galaxies at $z = 0$, and the right-hand side is the cumulative peak mass function of subhalos at $z = 0$. This matching assigns a tentative stellar mass, $M_{d,0}$, to a subhalo according to its peak mass. To take into account the scatter in the SMHM relation, we define for each subhalo a mass indicator, $M_{ind,0}$:

$$\log M_{ind,0} = \log M_{d,0} + \epsilon_0, \quad (2)$$

where ϵ_0 is a random number generated from some distribution function $P_0(\epsilon_0)$. In our model, we assume P_0 to be a normal distribution with zero mean and a dispersion of $\sigma_0 = 0.2$, as motivated by the SMHM relation inferred from observation (e.g. Yang et al. 2009; Behroozi et al. 2010; Li et al. 2012; Reddick et al. 2013; Wechsler & Tinker 2018). This mass is used to re-rank all subhalos. The stellar mass of a galaxy is then assigned to a subhalo of the same rank using

$$n(> M_{*,0}) = n(> M_{ind,0}). \quad (3)$$

The assigned stellar mass so obtained is denoted as $M_{sca,0}$, where ‘sca’ stands for ‘scatter’. Note that $M_{sca,0}$ has the same distribution as $M_{d,0}$, but is no longer a monotonic function of $M_{p,0}$ because of the nonzero scatter.

** want to induce noise to better match observed data, & have a better sense for the model*

- (ii) Perform the same SHAM procedure for galaxies at high z using

$$n(> M_{*,z}) = n(> M_{p,z}), \quad (4)$$

and we denote the assigned tentative stellar mass as $M_{d,z}$. To add scatter in the SMHM relation at high z , we again define a mass indicator, $M_{ind,z}$:

$$\log M_{ind,z} = \log M_{d,z} + \epsilon_z, \quad (5)$$

with ϵ_z being a random variable specified by a probability distribution function $P_z(\epsilon_z)$, and use it to re-rank subhalos. Since we want to link a $z = 0$ galaxy with a given stellar mass and subhalo mass to its progenitors at higher z , $P_z(\epsilon_z)$ is conditional on the descendant. For simplicity, we model P_z with a normal distribution, and describe the correlation with the descendant through a correlation coefficient ρ_z . Thus, we can write

$$P(\epsilon_z | M_{sca,0}, M_{d,0}) = \mathcal{N}\left(\frac{\rho_z \sigma_z \log(M_{sca,0}/M_{d,0})}{\sigma_0}, (1 - \rho_z^2) \sigma_z^2\right), \quad (6)$$

where $\mathcal{N}(\mu, \sigma)$ is a normal distribution with mean μ and standard deviation σ , and ρ_z describes the correlation between $\log(M_{ind,z}/M_{d,z})$ and $\log(M_{sca,0}/M_{d,0})$, i.e. the correlation of the deviation of the stellar mass from the tentative mass at z with that of its descendant at $z = 0$. We use results obtained from the TNG simulation to calibrate the model (see Appendix A). As shown in the left panel of Fig. A1, the scatter in the SMHM relation, σ_z , is independent of redshift, so that $\sigma_z \approx \sigma_0$ and

$$P(\epsilon_z | M_{sca,0}, M_{d,0}) = \mathcal{N}\left(\rho_z \log(M_{sca,0}/M_{d,0}), (1 - \rho_z^2) \sigma_0^2\right).$$

(7)

Thus, $\rho_z = 0$ implies that ϵ_z has a Gaussian distribution with zero mean and with dispersion equal to σ_0 , while $\rho_z = 1$ implies that $\epsilon_z = \log(M_{\text{sca},0}/M_{\text{d},0})$. The right panel of Fig. A1 shows that the correlation in the simulation can be described by

$$\rho_z = \exp(-0.83z), \quad (8)$$

and we adopt it for our model. We note that our results are insensitive to $\rho(z)$, as shown in Fig. A2. Finally, we perform the subhalo abundance matching using

$$n(> M_{*,z}) = n(> M_{\text{ind},z}) \quad (9)$$

to assign the stellar mass to a subhalo, and we denote this mass by $M_{\text{sca},z}$.

Once subhalos at different redshift are assigned with stellar masses, we link the stellar mass of a galaxy at $z = 0$ to that of its progenitors at higher z using its subhalo merger tree. We can then study the stellar mass distribution of the progenitors at a given z for galaxies selected at $z = 0$.

2.3 Assigning star-formation states to subhalos

Using the EAGLE simulation (Schaye et al. 2015), Clauwens et al. (2016) showed that the progenitor stellar mass of galaxies selected at $z \sim 0$ depends strongly on the star formation states of their descendants. Quiescent descendants on average have more massive progenitors than their star-forming counterparts, and this dependence is stronger for low-mass descendants. They also found that the evolving cumulative number density method proposed in Behroozi et al. (2013) cannot reproduce this trend, indicating that stellar mass alone is not sufficient to establish a reliable link between galaxies at different redshift. Some new properties must be included to improve the method. Here we add the star formation states of galaxies in the galaxy-halo connection. To this end, we use a conditional age distribution matching (CADM) method, which assumes a monotonic relation between the star-forming activity of a galaxy and some characteristic redshift describing the formation of its subhalo with fixed stellar mass and host halo mass (Hearin & Watson 2013; Hearin et al. 2014). We adopt a characteristic redshift, z_{starve} , similar to that used in Favole et al. (2022), where they defined z_{starve} as the maximum among z_{half} , z_{char} , and z_{acc} . Here z_{half} is the highest redshift when the halo mass of the main progenitor halo reaches half of the peak halo mass, M_p ; z_{char} is the highest redshift at which the mass of the main progenitor halo reaches $10^{12} h^{-1} M_\odot$; z_{acc} is the redshift at which the subhalo becomes a satellite subhalo and is set to 0 for all central subhalos. This definition of z_{starve} is able to reproduce the dependence of galaxy clustering on star formation rate (SFR) in the TNG simulation, as shown in Favole et al. (2022). Similar definitions have also been used to interpret the color and SFR dependence of galaxy clustering in observations (e.g. Hearin & Watson 2013; Hearin et al. 2014; Watson et al. 2015). We found that z_{half} is almost always greater than z_{acc} , and so we use

$$z_{\text{starve}} = \text{MAX}(z_{\text{char}}, z_{\text{half}}) \quad (10)$$

for our analysis.

We proceed to assign star formation states to subhalos at a given redshift through the following steps:

- (i) Apply the SHAM procedure described in § 2.2 to assign stellar masses to subhalos.

- (ii) For a fixed stellar mass and host halo mass bin, i.e. $(M_* \pm \Delta M_*/2, M_h \pm \Delta M_h/2)$, we calculate z_{starve} for subhalos in this bin, and identify a fraction of $F_q(M_* \pm \Delta M_*/2, M_h \pm \Delta M_h/2)$ subhalos with top z_{starve} as quiescent, while the remaining subhalos are identified as star-forming, where F_q is the quiescent fraction of galaxies in the corresponding stellar mass and host halo mass range.

After assigning stellar masses and star formation states to subhalos at different redshift, we can use subhalo merger trees to connect them and infer their redshift evolution. Note that the estimate of F_q as a function of stellar mass and host halo mass requires a complete galaxy group sample with reliable halo mass assignments. Currently, such samples are available only at $z \sim 0$.

3 TESTING THE METHOD WITH THE TNG SIMULATION

In this section, we use the IllustrisTNG simulation to test the performance of the method described above. As a check, we also apply our method to the EAGLE simulation, and the results are presented in Appendix B.

3.1 Simulation Data

We use the simulation data from IllustrisTNG (The Next Generation) (hereafter TNG, Nelson et al. 2019). TNG is a suite of gravo-magnetohydrodynamical cosmological simulations run with the moving-mesh code AREPO. Compared to the original Illustris, TNG has made a set of improvements, including an extension of the mass range for the simulated galaxies and halos, improved numerical and astrophysical modeling, and addressing identified shortcomings of the Illustris simulation (see Pillepich et al. 2018a; Weinberger et al. 2017, for the detailed modeling). TNG simulates the formation and evolution of galaxies from $z = 127$ to $z = 0$ based on a cosmology consistent with results in Planck Collaboration et al. (2016), where $\Omega_{\Lambda,0} = 0.6911$, $\Omega_{b,0} = 0.3089$, $\sigma_8 = 0.8159$, $n_s = 0.9667$ and $h = 0.6774$. TNG consists of a suite of ten simulations with different box sizes and resolutions. Here we use TNG100-1, which has 2×1820^3 resolution elements in a box with a side length of $75 h^{-1} \text{cMpc}$. The target baryon mass resolution is $1.4 \times 10^6 M_\odot$, and the dark matter particle mass is $7.5 \times 10^6 M_\odot$.

In the TNG simulation, dark matter halos were identified with the friends-of-friends (FoF) algorithm using dark matter particles. Substructures were identified with the SUBFIND algorithm using all types of particles (Springel et al. 2001). The baryonic components identified are considered as galaxies, and the dark matter components as subhalos. In each FoF halo, the central subhalo is defined as the subhalo located at the minimum of the gravitational potential, and the galaxy in it is referred to as the central galaxy. The remaining subhalos are defined as satellite subhalos, while galaxies in them as satellite galaxies.

Two different merger trees are provided by the TNG simulation: SUBLINK (Rodríguez-Gomez et al. 2015) and LHALOTREE (Springel et al. 2005). We use SUBLINK trees because of their easy accessibility. Once all the trees are built up, we can define the main progenitor of any halo (or galaxy) in the preceding snapshot as the one with the most massive progenitor history (See De Lucia & Blaizot 2007). By recursively identifying the main progenitor, we obtain a branch consisting of the main progenitors of the halo in question. This branch is referred to as the main branch of the halo.

The halo mass we use is the “top-hat” mass of the FoF halo within a radius within which the average overdensity is equal to that predicted

by the spherical collapse model (see Bryan & Norman 1998). The galaxy stellar mass we use is defined as the sum of the stellar particles within twice the stellar half-mass radius, $2R_*$, where R_* is calculated using all the stellar particles in the sub-halo (Pillepich et al. 2018b). The galaxy star formation rate is calculated by summing the birth-time-mass² of all the stellar particles formed in the last 200 Myrs within $2R_*$ and divide it by 200 Myrs (Donnari et al. 2019). Finally, galaxies are classified as quiescent when they satisfy

$$\frac{\text{SFR}}{M_*} < 10^{-11} h \text{ yr}^{-1}, \quad (11)$$

while the remaining galaxies are classified as star-forming.

To test the performance of our method, we applied it to the TNG simulation to infer the stellar mass evolution histories and compared them with the results obtained directly from galaxy merger trees in the simulation. To begin with, we calculated the stellar mass function at each snapshot and assigned stellar mass to subhalos using the method described in § 2.2. We then calculated the quiescent fraction as a function of the stellar mass and host halo mass of galaxies at $z = 0$ and assigned star formation states to subhalos using the method described in § 2.3. Finally, we calculated the distribution and redshift evolution of the stellar mass of the progenitor mass conditioned on the stellar mass and star formation states of descendant galaxies at $z = 0$, and compared the results with those obtained directly from the TNG simulation. The performances of the method are presented in relevant subsections in the following.

3.2 Stellar mass distributions of progenitors

In the current Λ CDM paradigm, cosmic structures form hierarchically, and so do galaxies. This hierarchical formation of galaxies can be described by the distribution of the galaxy population, i.e. the stellar mass function, at $z = 0$ and the distribution of their progenitors at higher z , i.e. the progenitor normalized stellar mass function (PNSMF). The PNSMF is defined as the number of progenitor galaxies at a given redshift, as a function of the stellar mass ratio, $M_*/M_{*,0}$, for a given set of descendant galaxies with the same stellar mass $M_{*,0}$. We first examine the performance of our method in recovering this statistic, and the result is presented in Fig. 2, where solid lines are the results obtained directly from galaxy merger trees in the TNG simulation and dashed lines are predictions of our method. Results are shown separately for the total (upper panels), quiescent (middle panels), and star-forming populations (lower panels). As one can see, the PNSMF is dominated by low-mass galaxies and declines toward the massive end at high redshift. When evolved to low redshift, the PNSMF becomes more dominated by massive progenitors. This trend is consistent with the hierarchical scenario of galaxy assembly where low-mass galaxies formed at high redshift are assembled into more massive descendants at lower redshift, and low-mass descendants are assembled earlier than more massive ones. The redshift evolution of the PNSMF in the simulation is well reproduced by our method over the entire stellar mass range covered by the TNG simulation, and for both quiescent and star-forming populations. We also test the performance of our method on the EAGLE simulation in Appendix B, and Fig. B1 confirms that our method is able to recover the PNSMFs properly.

² The birth-time-mass of each stellar particle is different from its current mass due to the mass loss through stellar wind.

3.3 The growth of galaxies

Although tracing all the progenitor galaxies can provide a more complete description of galaxy assembly histories, a simpler and yet illuminating description can be obtained by examining how galaxies grow along their main branches. Fig. 3 shows the stellar mass evolution of the main progenitors for galaxies of different present-day mass hosted by halos in three mass ranges, as indicated by $\log M_0$ in each panel. The results for different descendant stellar mass bins are shifted vertically for clarity. Shaded regions are obtained from galaxy merger trees of the TNG simulation, and symbols are the predictions of our method. Both errors are estimated using the bootstrap method. Results are shown separately for the total, quiescent and star-forming populations of the descendant galaxies, as black, red, and blue lines, respectively. It is clear from the figure that our method can accurately reproduce the stellar mass growth of the main progenitors for descendant galaxies of different stellar masses and different host halo mass. Our method also works well for quiescent descendants over the entire stellar mass and redshift ranges, and for star-forming descendants of low-mass descendants at $z < 2$. Our method underestimates the progenitor stellar mass for massive star-forming galaxies at $z \gtrsim 2$, especially in low-mass halos. This suggests that star formation activities in massive galaxies are not fully determined by the assembly histories of dark matter halos (e.g. Chen et al. 2021). We also test the performance of our method using the EAGLE simulation in Appendix B, and Fig. B2 shows again that our method works well in recovering the stellar mass growth of main progenitors in the EAGLE simulation. Note that each of the descendant stellar mass bins used for our presentations overlaps with its adjacent bins. This choice is to obtain better statistics for each bin and provides more options to use the data. If one is to use the data to constrain models, only data for independent mass bins should be used.

4 APPLICATIONS TO REAL OBSERVATIONS

The previous section shows that our method is capable of modeling the formation histories of galaxies with different masses and star formation states. Here we apply our method to observations to infer the stellar mass assembly histories of galaxies in the real Universe.

4.1 Observational data

As shown in Section 2, assigning stellar masses to subhalos requires stellar mass functions from $z = 0$ to the redshift we want to probe. Here we use the stellar mass function measurements from the SDSS-GALEX and COSMOS2015 catalogues (Moustakas et al. 2013; Davidzon et al. 2017).³ Stellar masses are estimated using the stellar population synthesis model of Bruzual & Charlot (2003), the dust model of Calzetti et al. (2000), and the initial mass function of Chabrier (2003). The cumulative stellar mass functions obtained this way for galaxies at different redshift are presented in Fig. 4.

In order to assign star formation states to subhalos, we also need to know the fraction of quiescent galaxies as a function of stellar mass and host halo mass. The information of host halo mass can be obtained by grouping galaxies into clusters and groups that can be

³ We note that the stellar mass function measurement in Moustakas et al. (2013) suffers from systematic effects in photometry and uses a stellar mass estimate that is different from Davidzon et al. (2017). To maintain consistency in observational data, we adopt the re-calibrated results in Behroozi et al. (2019) where an attempt was made to deal with these issues.

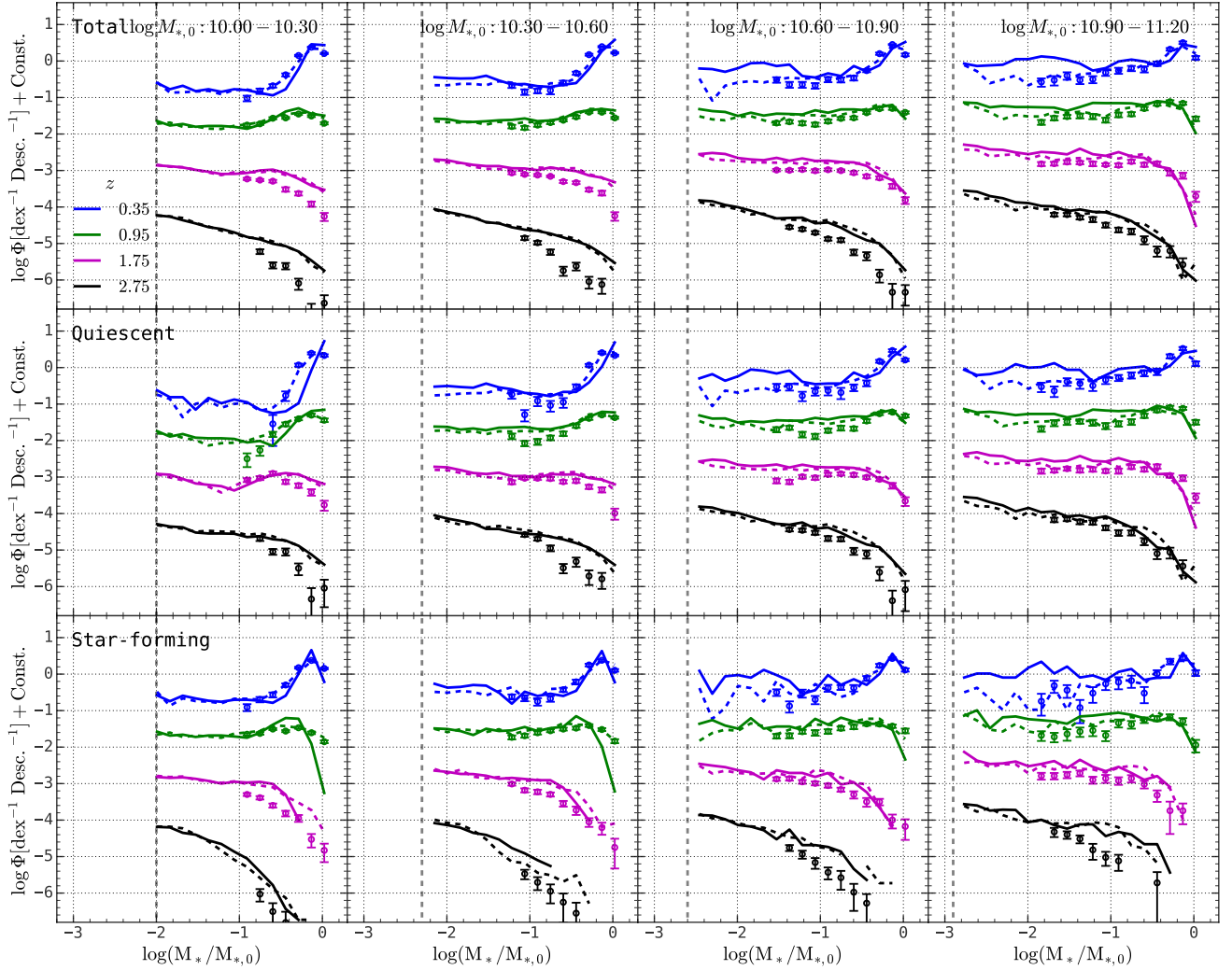


Figure 2. Progenitor normalized stellar mass functions for different descendant stellar mass bins (*different columns*) and different descendant star-formation states (*different rows*) at four redshift snapshots. The solid lines are extracted from galaxy merger trees of the TNG simulation, dashed lines are the results of applying our method to the TNG simulation. Symbols are the results of applying our method to real observation with error bars calculated using the bootstrap method. The vertical dashed lines indicate the minimal stellar mass resolved by the TNG simulation. Here y -values are shifted for clarity.

used to represent host halos of galaxies. At the present, this can be done reliably only for the local Universe (e.g. [Yang et al. 2007](#); [Wang et al. 2020](#)). Nevertheless, the data available at $z \sim 0$ are sufficient to study the stellar mass evolution conditioned on descendant properties at $z \sim 0$, as is done in § 3. Here we use the criterion in equation (11) to separate quiescent galaxies from their star-forming counterparts, where the star formation rate measurements come from MPA-JHU DR7 ⁴ ([Brinchmann et al. 2004](#)), and the quiescent fraction as a function of stellar mass and host halo mass is presented in Fig. 5. We note that the quiescent fractions have been previously obtained with the SDSS galaxy sample (e.g. [Wetzel et al. 2012](#); [Hirschmann et al. 2014](#); [Wang et al. 2018](#); [Li et al. 2020](#)), but different studies differ to varying degrees, particularly at low stellar mass and high halo mass due to different criteria to separate quiescent and star-forming populations. It is thus necessary to apply the same criterion for both

observational measurements and theoretical models for a meaningful comparison, as the case in the present work. Tests show that we’re able to reproduce the measurements in the literature if exactly the same criteria are adopted.

To apply our method to observational data, we first assign stellar mass to subhalos at nine snapshots following the procedures in § 2.2, where each snapshot is selected to match the middle value of the redshift interval in which the stellar mass function is measured from observational data (see Fig. 4). We then apply the method in § 2.3 to assign star formation states to subhalos at $z \sim 0.1$ using the observed quiescent fraction shown in Fig. 5. Finally, we calculate the distribution and redshift evolution of the progenitor stellar mass for descendant galaxies of different stellar mass, halo mass, and star formation states. The results are presented in subsequent subsections. Note that the lowest redshift we can probe is $z \sim 0.1$, since $M_{*,0}$ and M_0 used in observational results are actually measured at $z \sim 0.1$.

⁴ <http://www.mpa-garching.mpg.de/SDSS/DR7/>

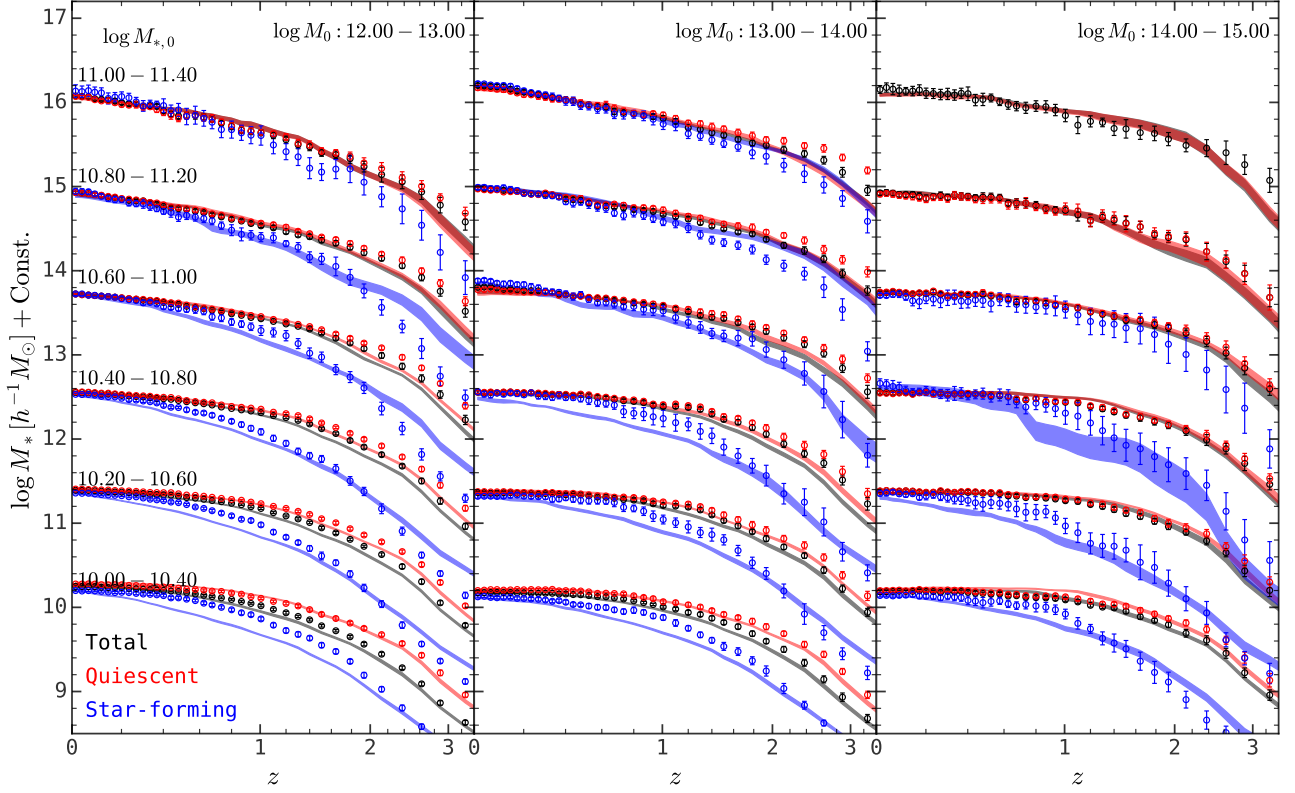


Figure 3. Median stellar mass evolution of main progenitor galaxies in the TNG simulation. Results are presented in bins of descendant stellar mass and descendant halo mass. Red/blue/black colors are for quiescent/star-forming/total populations of descendant galaxies. Filled regions are the results derived from galaxy merger trees in the TNG simulation. Symbols are the results of our method applied to the TNG simulation. All the errors are calculated using the bootstrap method.

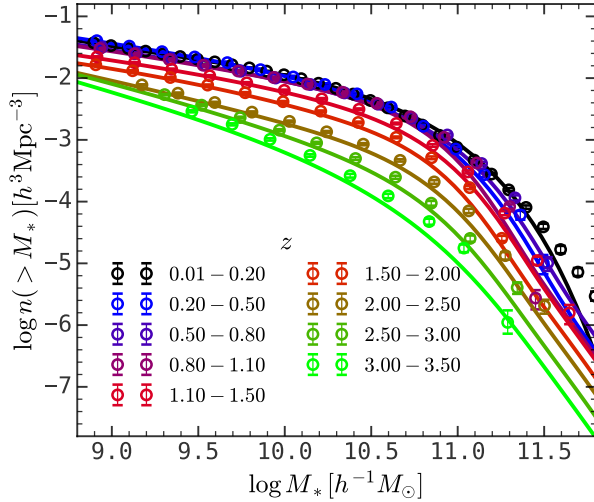


Figure 4. The cumulative stellar mass function for galaxies at $0.01 < z < 3.50$ from the SDSS-GALEX and COSMOS2015 catalogues (Moustakas et al. 2013; Davidzon et al. 2017). Circles with error bars are measurements, and solid lines are fitting results (Davidzon et al. 2017).

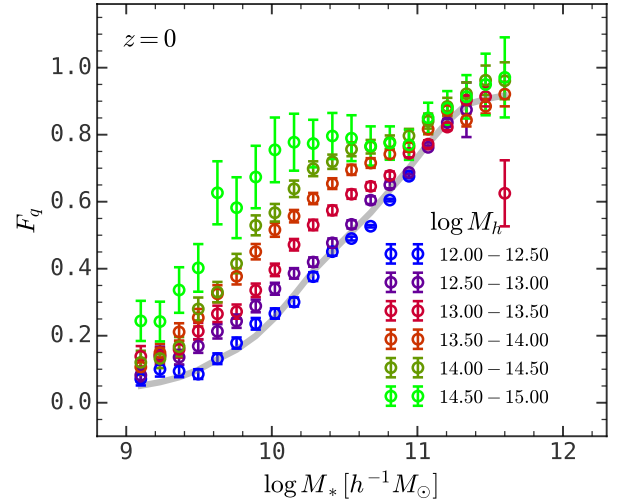


Figure 5. Quiescent fraction of galaxies at $0.01 < z < 0.20$ calculated from the MPA-JHU DR7 catalog (Brinchmann et al. 2004) and the group catalogue in Yang et al. (2007). Circles with error bars are for galaxies with different host halo masses, and gray shaded regions are for all of the galaxies.

4.2 Stellar mass evolution since $z \sim 3$

Circles in Fig. 2 show PNSMFs obtained from our observational data, with error bars obtained using the bootstrap method. The overall trends of the observational results are similar to those given by the TNG simulation, except for some noticeable discrepancies at high z for descendants of low masses. These discrepancies are expected, as the TNG simulation over-predicts the stellar mass function at $1.0 \lesssim z \lesssim 3.0$ (Pillepich et al. 2018b).

Fig. 6 shows the median stellar mass evolution of main progenitor galaxies for descendants with different stellar mass, halo mass, and star formation state. Circles show the results obtained by applying our method to the observational data, where the horizontal error bars show the redshift bins and the vertical error bars show the standard deviation calculated from bootstrap samples.

We can see that the progenitors of descendant galaxies of a given stellar mass are less massive in lower-mass halos, as shown by the black symbols in Fig. 6, indicating that these galaxies evolve more rapidly over the redshift range covered. For example, consider the stellar mass growth from $z \sim 2$ to $z = 0$. For massive galaxies with $M_{*,0} \sim 10^{11} h^{-1} M_{\odot}$, those residing in halos with $M_0 \sim 10^{12} - 10^{13} h^{-1} M_{\odot}$ have increased their stellar mass by a factor of ~ 7 , while those with $M_0 \gtrsim 10^{14} M_{\odot}$ have increased only a factor of ~ 2.5 . For lower-mass galaxies with $M_{*,0} \sim 10^{10} h^{-1} M_{\odot}$, the stellar mass growth factors for galaxies residing in low-mass and massive halos are ~ 12 and ~ 5 , respectively. Roughly speaking, galaxies that end up in low-mass descendant halos grow ~ 2.5 times as fast as those that end up in massive halos.

In general, for similar descendant stellar mass and descendant halo mass, star-forming galaxies at $z \sim 0$ have progenitors that are less massive than those of their quiescent counterparts, indicating that they grow more rapidly. For example, between $z \sim 1.8$ and $z \sim 0$, low-mass star-forming galaxies grow faster than their quiescent counterparts by a factor of ~ 4 , while this factor is ~ 2 for massive descendant galaxies. Both factors depend only weakly on the host halo mass. These results indicate that the dependence of stellar mass growth on descendant halo mass is mainly due to the fact that the fraction of quiescent galaxies is higher in more massive halos at $z \sim 0$.

We can also quantify the stellar mass growth by identifying the epoch when a galaxy has obtained a certain fraction of its final stellar mass. Fig. 7 shows the lookback time when the main progenitor has accumulated 10% ($t_{*,10\%}$) and 50% ($t_{*,50\%}$) of its final stellar mass, respectively. Results are shown for star-forming and quiescent descendant galaxies with different stellar masses and host halo masses. Overall, quiescent descendant galaxies formed earlier than their star-forming counterparts by $\sim 1 - 2$ Gyr depending on the descendant stellar mass and descendant halo mass. It is clear that galaxies with the same stellar mass but hosted by more massive descendant halos formed earlier than the ones that end up in low-mass halos, and this halo mass dependence appears to be stronger at higher stellar mass. The only exception is that the halo mass dependence is rather weak at the lowest stellar mass bin, where star-forming galaxies in massive halos appear to be as young as their counterparts in low-mass halos. Some of the galaxies in this population may be accreted into massive halos only recently, and their evolution may not yet have been affected by the cluster environment (e.g. Wetzel et al. 2013).

The general trends presented above are consistent with the results in both the TNG and EAGLE simulations (See Figs. 3 and B2). They are not revealed in previous methods because these methods neglect the dependence of the stellar mass evolution on descendant halo mass and descendant star formation state.

In the simple formalism described in Behroozi et al. (2013), the stellar mass evolution of main progenitors is followed by using the cumulative number density as an equivalent of the stellar mass:

$$\log \left(\frac{n_z(> M_*)}{n_0(> M_{*,0})} \right) = \text{Slope} \times z, \quad (12)$$

where the cumulative number density is defined as

$$n_z(> M_*) = \int_{M_*}^{\infty} \Phi_z(M') dM', \quad (13)$$

with $\Phi_z(M_*)$ being the stellar mass function at redshift z . The observed relations between M_* and $n(> M_*)$ at different redshift are shown in Fig. 4. In this way, one can use a single parameter, the Slope defined in equation (12), to describe the main progenitor stellar mass evolution for given descendant galaxies. Using the cumulative number density to replace the stellar mass has the advantage that it is less affected by systematic uncertainties in the stellar mass estimate (Conroy 2013).

Fig. 8 shows the redshift evolution of the cumulative number density of main progenitor galaxies. Each evolution trajectory is fitted with a linear function given by equation (12), and shown as solid lines. We emphasize again that the evolution of the cumulative number density is mathematically equivalent to the evolution in stellar mass. The advantage of going through an intermediate step of using the cumulative number density is that it can be described well by the simple linear function, equation (12), specified by a slope. Overall, the cumulative number density increases faster with increasing z for star-forming galaxies than their quiescent counterparts, implying that quiescent galaxies have more massive progenitors than star-forming galaxies.

To see this more clearly, we plot in Fig. 9 the slope defined in equation (12) as a function of descendant properties. For reference, the black solid line in the left panel shows the result obtained by using the evolving number density method of Behroozi et al. (2013). In this case, the dependence on the descendant stellar mass, $M_{*,0}$, is weak, consistent with the result of Behroozi et al. (2013), shown with the gray horizontal line. Inspecting the dependence on both the descendant stellar mass, $M_{*,0}$, and the descendant halo mass, M_0 , we see that the slope parameter has a modest dependence on host halo mass: at fixed stellar mass the galaxies in massive halos have a smaller slope, and thus have evolved more slowly. The middle and right panels show results separately for the star-forming and quiescent descendants. It is clear that, on average, the slope parameter for quiescent descendant galaxies is smaller than their star-forming counterparts, indicating a slower growth of stellar mass in quiescent galaxies over the redshift range being considered. Moreover, the dependence on the host halo mass in the middle and right panels is somewhat weaker than that in the left panel, indicating that the dependence on the host halo mass in the left panel is partly caused by the dependence of the quiescent fraction on the host halo mass. These results also show that, in order to recover the details of the stellar mass growth of galaxies, it is important to control the star formation and halo properties of galaxies in addition to the stellar mass of galaxies (e.g. Clauwens et al. 2016).

To show the difference between our results and previous ones more clearly, we plot our fitting results as solid lines in Fig. 6 using the relation between M_* and $n(> M_*)$ shown in Fig. 4. In addition, we also plot the results of Behroozi et al. (2013) (Slope = 0.16) as dashed lines, and results of the constant cumulative number density (CCND) method (Slope = 0) as dashed-dotted lines in Fig. 6. Our method predicts more massive main progenitor galaxies for quiescent descendants than for their star-forming counterparts. In addition, our

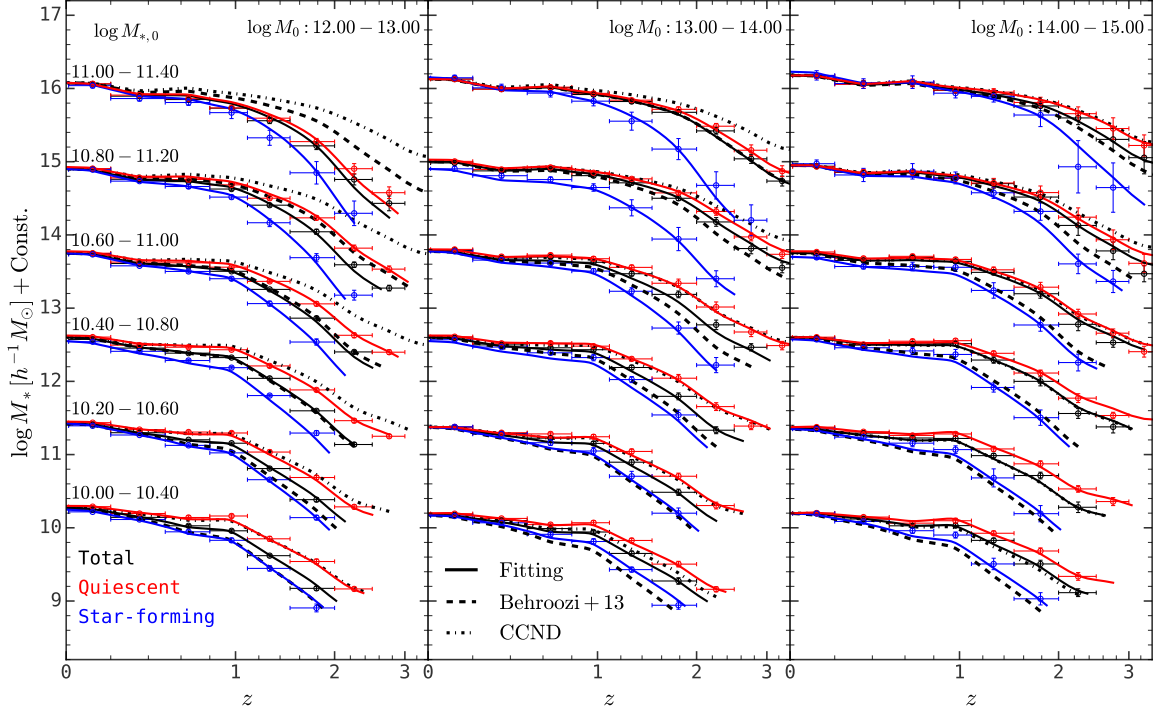


Figure 6. Median stellar mass evolution of main progenitor galaxies derived from the observational data with our method. Results are presented in bins of descendant stellar mass, $M_{*,0}$, and descendant halo mass, M_0 . Red/blue/black colors are for quiescent/star-forming/total populations of descendant galaxies. Circles are the direct results of our method, with horizontal error bars showing the corresponding redshift bins and vertical error bars showing the standard deviations estimated with the bootstrap method. Solid lines are results derived from our linear fitting to the evolution of the cumulative number density (See equation (12)). Dashed lines are the results in Behroozi et al. (2013). Dash-dotted lines are the results derived with the constant cumulative number density (CCND) method (see van Dokkum et al. 2010).

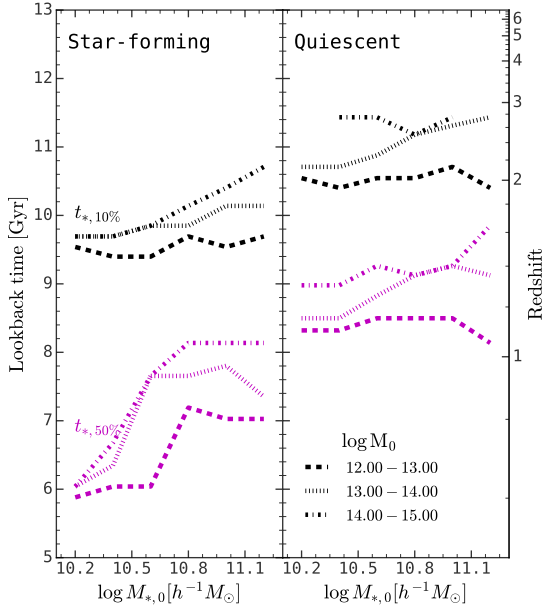


Figure 7. Galaxy formation time defined as the lookback time that 10% (black) and 50% (magenta) of the final stellar mass is assembled into the main progenitor. Results are presented for star-forming (left panel) and quiescent (right panel) descendant galaxies with different stellar mass and halo mass.

method also predicts more massive main progenitors for descendants in massive halos. This is expected because stellar mass growth is suppressed in dense regions at the present day. Both of these trends are also found in the TNG and EAGLE simulations as shown below, but they are not recovered by previous methods since they do not consider the dependence of the stellar mass growth on the host halo mass and star formation state of descendant galaxies.

4.3 Comparison between simulations and observation

In Fig. 10, we compare the stellar mass evolution of main progenitor galaxies obtained from observational data with results in the TNG and EAGLE simulations. Here we only show the comparison in the descendant halo mass bin of $13 < \log(M_0/[h^{-1}M_\odot]) < 14$ since other bins have similar trends. For massive descendant galaxies with $M_{*,0} > 10^{11}M_\odot$, both simulations can reproduce the evolution trend for the quiescent and total populations of descendant galaxies. However, there is a discrepancy for star-forming descendants at $z \gtrsim 1.5$. This discrepancy arises because both simulations overpredict the stellar mass function at high- z (Pillepich et al. 2018b; Furlong et al. 2015). The two simulations also overpredict the progenitor stellar mass for low-mass descendants regardless of their star formation states, again because they overestimate the stellar mass function at high z .

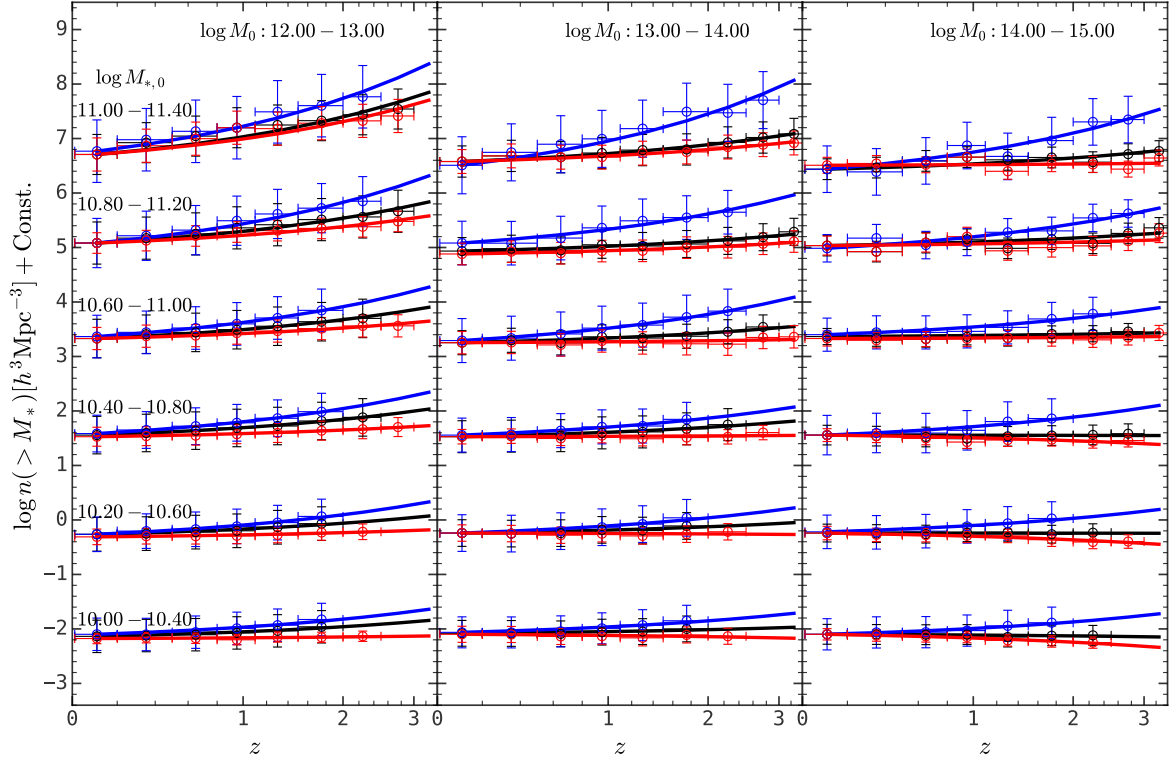


Figure 8. Median cumulative number density evolution of main progenitor galaxies derived from the observational data with our method. Results are presented in bins of descendant stellar mass, $M_{*,0}$, and descendant halo mass, M_0 . Red/blue/black colors are for quiescent/star-forming/total populations of descendant galaxies. Circles with error bars are derived from our method, where the horizontal error bars show the redshift bins, and the vertical error bars are derived with the bootstrap method. Solid lines are linear fitting results (See equation (12)). Note that this figure can be converted into the solid lines and symbols in Fig. 6 using the cumulative stellar mass function shown in Fig. 4.

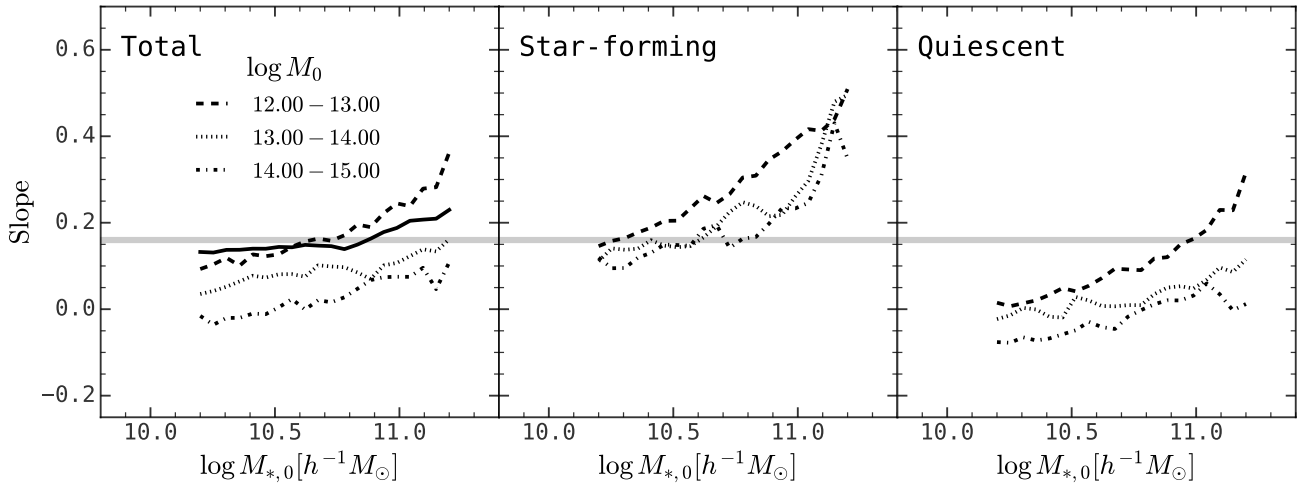


Figure 9. The slope of the redshift evolution in the cumulative number density (See equation (12)) and its dependence on descendant stellar mass, descendant halo mass, and descendant star formation state. The horizontal line is the result obtained in Behroozi et al. (2013) using the evolving cumulative number density method, i.e. Slope = 0.16, which neglects the dependence on descendant halo mass and descendant star formation state. As a check, we also implement the same evolving cumulative number density method in Behroozi et al. (2013) and the result is shown as the black solid line in the first panel, which is consistent with the horizontal line.

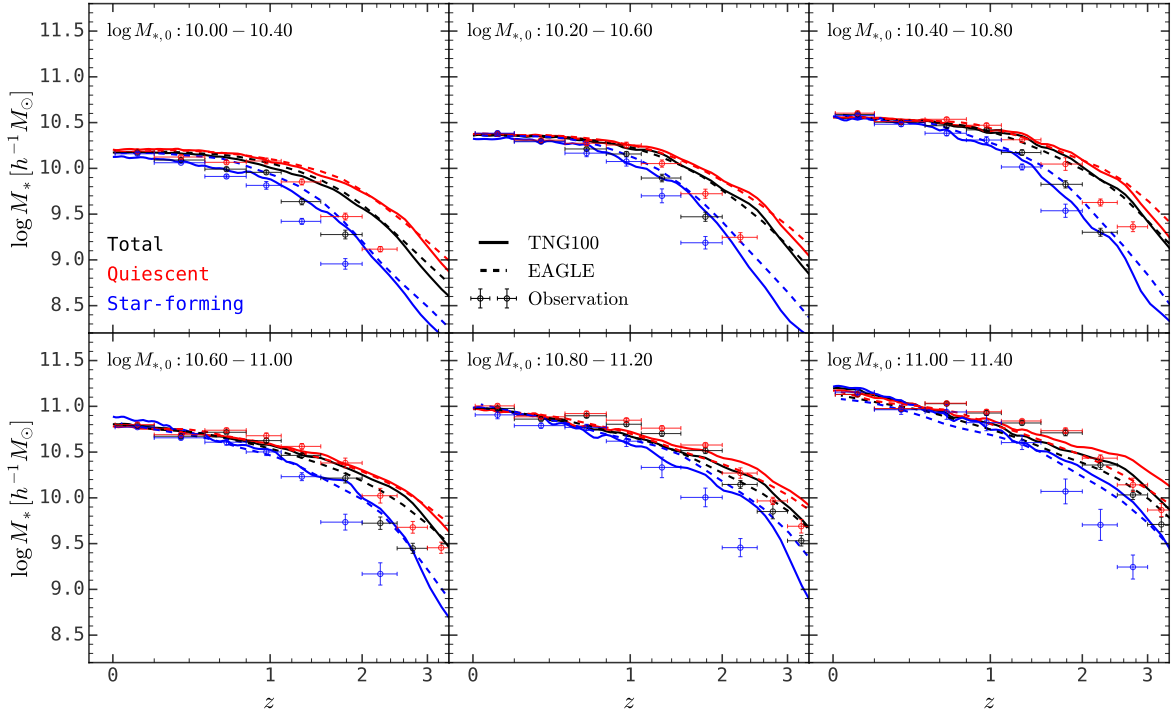


Figure 10. Comparison of the median stellar mass evolution of main progenitor galaxies obtained by applying our method to simulations and observation. Here we only present results for galaxies with descendant halo mass of $13 \leq \log(M_0/[h^{-1}M_\odot]) < 14$ and omit results in other mass ranges since they are very similar. Circles with error bars are derived from observational data. Solid and dashed lines are obtained from galaxy merger trees in the TNG and EAGLE simulations, respectively. Red/blue/black colors are for quiescent/star-forming/total populations of descendant galaxies.

5 SUMMARY

Connecting progenitor and descendant galaxies across cosmic time statistically has proven to be a promising way to investigate galaxy evolution (e.g. Brown et al. 2007; van Dokkum et al. 2010; van de Voort 2016; Behroozi et al. 2013; Leja et al. 2013; Jaacks et al. 2016; Hill et al. 2017). Previous investigations only used the stellar mass of galaxies to establish this connection, neglecting the dependence on other properties, such as star formation activities and host halo mass of descendant galaxies. In the present paper, we propose a general framework, which leverages galaxy-halo connections that have been established in the past, to connect galaxies across cosmic time using subhalo merger trees expected from the current model of structure formation. Our main results are summarized as follows:

(i) We tested our method by applying it to the TNG and EAGLE cosmological simulations. Our results show that our method can properly recover the progenitor stellar mass distribution up to $z \sim 3$ for star-forming and quiescent descendant galaxies with different stellar masses and host halo masses. Our method can also recover the stellar mass growth along the main branches of galaxies.

(ii) Applying our method to observational data, we derived the stellar mass assembly histories since $z \sim 3$ for galaxies in the local Universe, including the stellar mass evolution along the main branch.

(iii) We found that the stellar mass growth depends strongly on the descendant halo mass at $z = 0$. Since $z \sim 1.8$, massive descendant galaxies in low-mass halos have increased their stellar mass by a factor of ~ 7 , while low-mass descendant galaxies have increased their masses by a factor of ~ 12 . In massive descendant halos, the stellar mass growth for massive and low-mass descendant galaxies is

about factors of 2.5 and 5, respectively. Thus, galaxies that end up in present low-mass groups accumulate their stellar mass ~ 2.5 times as fast as those that end up in massive clusters.

(iv) We found that the stellar mass growth also depends on the current star formation activity of descendant galaxies. From $z \sim 2$ to $z \sim 0$, the stellar mass growth rate for star-forming descendant galaxies is about 2 \sim 4 times faster than their quiescent counterparts, quite independent of descendant halo mass. This suggests that the dependence on the host halo mass is mainly driven by the correlation between the quiescent fraction and the host halo mass.

(v) We found that the stellar mass evolution can be well described by a linear function in the logarithm of the cumulative number density, as in equation (12), for descendant galaxies with given stellar mass, star-formation state, and host halo mass. The resulting parameter, Slope, also shows a strong dependence on both the descendant star formation state and descendant halo mass. The dependence on the descendant halo mass becomes weaker when the descendant star formation state is fixed. These trends are consistent with the analysis using stellar mass alone.

(vi) We compared the stellar mass evolution derived from observation with results in the TNG and EAGLE simulations. We found that both simulations over-predict the progenitor stellar mass for low-mass descendant galaxies, because both simulations over-predict the stellar mass functions at high z .

Again, it is important to take into account the potential dependencies of the evolution on descendant star formation activities and descendant halo mass, and the method proposed here provides a more accurate framework for such modeling.

ACKNOWLEDGEMENTS

The authors thank the anonymous referee for their helpful comments that improved the quality of the manuscript. This work is supported by the National Key R&D Program of China (grant No. 2018YFA0404502, 2018YFA0404503), and the National Science Foundation of China (grant Nos. 11821303, 11973030, 11673015, 11733004, 11761131004, 11761141012). The authors acknowledge the Tsinghua Astrophysics High-Performance Computing platform at Tsinghua University for providing computational and data storage resources that have contributed to the research results reported within this paper.

Funding for the SDSS and SDSS-II has been provided by the Alfred P. Sloan Foundation, the Participating Institutions, the National Science Foundation, the U.S. Department of Energy, the National Aeronautics and Space Administration, the Japanese Monbukagakusho, the Max Planck Society, and the Higher Education Funding Council for England. The SDSS Web Site is <http://www.sdss.org/>.

The SDSS is managed by the Astrophysical Research Consortium for the Participating Institutions. The Participating Institutions are the American Museum of Natural History, Astrophysical Institute Potsdam, University of Basel, University of Cambridge, Case Western Reserve University, University of Chicago, Drexel University, Fermilab, the Institute for Advanced Study, the Japan Participation Group, Johns Hopkins University, the Joint Institute for Nuclear Astrophysics, the Kavli Institute for Particle Astrophysics and Cosmology, the Korean Scientist Group, the Chinese Academy of Sciences (LAMOST), Los Alamos National Laboratory, the Max-Planck-Institute for Astronomy (MPIA), the Max-Planck-Institute for Astrophysics (MPA), New Mexico State University, Ohio State University, University of Pittsburgh, University of Portsmouth, Princeton University, the United States Naval Observatory, and the University of Washington.

DATA AVAILABILITY

The data underlying this article will be shared on reasonable request to the corresponding author. The computation in this work is supported by the HPC toolkit **HIPP** at <https://github.com/ChenYangyao/hipp>.

REFERENCES

Baldry I. K., et al., 2012, *Monthly Notices of the Royal Astronomical Society*, pp no–no
 Behroozi P. S., Conroy C., Wechsler R. H., 2010, *The Astrophysical Journal*, 717, 379
 Behroozi P. S., Marchesini D., Wechsler R. H., Muzzin A., Papovich C., Stefanon M., 2013, *The Astrophysical Journal*, 777, L10
 Behroozi P., Wechsler R. H., Hearin A. P., Conroy C., 2019, *Monthly Notices of the Royal Astronomical Society*, 488, 3143
 Benson A. J., 2010, *Physics Reports*, 495, 33
 Brinchmann J., Charlot S., White S. D. M., Tremonti C., Kauffmann G., Heckman T., Brinkmann J., 2004, *Monthly Notices of the Royal Astronomical Society*, 351, 1151
 Brown M. J. I., Dey A., Jannuzi B. T., Brand K., Benson A. J., Brodwin M., Croton D. J., Eisenhardt P. R., 2007, *The Astrophysical Journal*, 654, 858
 Bruzual G., Charlot S., 2003, *Monthly Notices of the Royal Astronomical Society*, 344, 1000
 Bryan G. L., Norman M. L., 1998, *ApJ*, 495, 80
 Calzetti D., Armus L., Bohlin R. C., Kinney A. L., Koornneef J., Storchi-Bergmann T., 2000, *The Astrophysical Journal*, 533, 682

Chabrier G., 2003, *Publications of the Astronomical Society of the Pacific*, 115, 763
 Chen Y., Mo H. J., Li C., Wang H., Yang X., Zhou S., Zhang Y., 2019, *The Astrophysical Journal*, 872, 180
 Chen Y., Mo H. J., Li C., Wang K., 2021, *Monthly Notices of the Royal Astronomical Society*, 504, 4865
 Clauwens B., Franx M., Schaye J., 2016, *Monthly Notices of the Royal Astronomical Society: Letters*, 463, L1
 Collaboration P., et al., 2014, *Astronomy and Astrophysics*, 571, A1
 Conroy C., 2013, *Annual Review of Astronomy and Astrophysics*, 51, 393
 Conroy C., Wechsler R. H., 2009, *The Astrophysical Journal*, 696, 620
 Conroy C., Wechsler R. H., Kravtsov A. V., 2006, *The Astrophysical Journal*, 647, 201
 Contreras S., Angulo R. E., Zennaro M., 2021, *MNRAS*, 508, 175
 Croton D. J., et al., 2006, *MNRAS*, 365, 11
 Davidzon I., et al., 2017, *Astronomy & Astrophysics*, 605, A70
 De Lucia G., Blaizot J., 2007, *Monthly Notices of the Royal Astronomical Society*, 375, 2
 Donnari M., et al., 2019, *Monthly Notices of the Royal Astronomical Society*, 485, 4817
 Driver S. P., et al., 2022, *Monthly Notices of the Royal Astronomical Society*, 513, 439
 Favole G., Montero-Dorta A. D., Artale M. C., Contreras S., Zehavi I., Xu X., 2022, *Monthly Notices of the Royal Astronomical Society*, 509, 1614
 Furlong M., et al., 2015, *Monthly Notices of the Royal Astronomical Society*, 450, 4486
 Gerke B. F., et al., 2007, *Monthly Notices of the Royal Astronomical Society*, 376, 1425
 Guo Q., White S., Li C., Boylan-Kolchin M., 2010, *Monthly Notices of the Royal Astronomical Society*
 Guo Q., et al., 2011, *Monthly Notices of the Royal Astronomical Society*, 413, 101
 Hearin A. P., Watson D. F., 2013, *Monthly Notices of the Royal Astronomical Society*, 435, 1313
 Hearin A. P., Zentner A. R., Berlind A. A., Newman J. A., 2013, *Monthly Notices of the Royal Astronomical Society*, 433, 659
 Hearin A. P., Watson D. F., Becker M. R., Reyes R., Berlind A. A., Zentner A. R., 2014, *Monthly Notices of the Royal Astronomical Society*, 444, 729
 Henriques B. M. B., White S. D. M., Thomas P. A., Angulo R., Guo Q., Lemson G., Springel V., Overzier R., 2015, *Monthly Notices of the Royal Astronomical Society*, 451, 2663
 Hill A. R., et al., 2017, *The Astrophysical Journal*, 837, 147
 Hirschmann M., De Lucia G., Wilman D., Weinmann S., Iovino A., Cucciati O., Zibetti S., Villalobos Á., 2014, *MNRAS*, 444, 2938
 Jaacks J., Finkelstein S. L., Nagamine K., 2016, *The Astrophysical Journal*, 817, 174
 Kang X., Jing Y. P., Mo H. J., Börner G., 2005, *The Astrophysical Journal*, 631, 21
 Kipper R., Tamm A., Tempel E., de Propriis R., Ganeshiah Veena P., 2021, *Astronomy and Astrophysics*, 647, A32
 Leja J., van Dokkum P., Franx M., 2013, *The Astrophysical Journal*, 766, 33
 Li C., White S. D. M., 2009, *Monthly Notices of the Royal Astronomical Society*, 398, 2177
 Li C., Kauffmann G., Jing Y. P., White S. D. M., Börner G., Cheng F. Z., 2006, *Monthly Notices of the Royal Astronomical Society*, 368, 21
 Li C., Jing Y. P., Mao S., Han J., Peng Q., Yang X., Mo H. J., van den Bosch F., 2012, *ApJ*, 758, 50
 Li C., Wang L., Jing Y. P., 2013, *The Astrophysical Journal*, 762, L7
 Li P., Wang H., Mo H. J., Wang E., Hong H., 2020, *ApJ*, 902, 75
 Lilly S. J., et al., 2009, *The Astrophysical Journal Supplement Series*, 184, 218
 Lu Z., Mo H. J., Lu Y., Katz N., Weinberg M. D., van den Bosch F. C., Yang X., 2014, *Monthly Notices of the Royal Astronomical Society*, 439, 1294
 Maiolino R., et al., 2020, *Published in The Messenger vol. 180*, pp. 24–29, 6 pages
 Mo H. J., Mao S., White S. D. M., 1999, *Monthly Notices of the Royal Astronomical Society*, 304, 175

Mo H., van den Bosch F. C., White S., 2010, *Galaxy Formation and Evolution*
 Mosser B. P., Somerville R. S., Maulbetsch C., van den Bosch F. C., Macciò
 A. V., Naab T., Oser L., 2010, *The Astrophysical Journal*, 710, 903
 Moustakas J., et al., 2013, *The Astrophysical Journal*, 767, 50
 National Academies of Sciences and Medicine E., 2021, *Pathways to Discov-
 ery in Astronomy and Astrophysics for the 2020s*, doi:10.17226/26141.

Nelson D., et al., 2019, *Computational Astrophysics and Cosmology*, 6, 2
 Pillepich A., et al., 2018a, *Monthly Notices of the Royal Astronomical Soci-
 ety*, 473, 4077
 Pillepich A., et al., 2018b, *Monthly Notices of the Royal Astronomical Soci-
 ety*, 475, 648
 Planck Collaboration et al., 2016, *Astronomy & Astrophysics*, 594, A13
 Reddick R. M., Wechsler R. H., Tinker J. L., Behroozi P. S., 2013, *The
 Astrophysical Journal*, 771, 30
 Rodriguez-Gomez V., et al., 2015, *Monthly Notices of the Royal Astronomical
 Society*, 449, 49
 Schaye J., et al., 2015, *Monthly Notices of the Royal Astronomical Society*,
 446, 521
 Somerville R. S., Primack J. R., 1999, *MNRAS*, 310, 1087
 Springel V., White S. D. M., Tormen G., Kauffmann G., 2001, *Monthly
 Notices of the Royal Astronomical Society*, 328, 726
 Springel V., Di Matteo T., Hernquist L., 2005, *Monthly Notices of the Royal
 Astronomical Society*, 361, 776
 Takada M., et al., 2014, *Publications of the Astronomical Society of Japan*,
 66, R1
 Tal T., et al., 2014, *The Astrophysical Journal*, p. 11
 Tomczak A. R., et al., 2014, *The Astrophysical Journal*, 783, 85
 Torrey P., et al., 2015, *Monthly Notices of the Royal Astronomical Society*,
 454, 2770
 Torrey P., Wellons S., Ma C.-P., Hopkins P. F., Vogelsberger M., 2017,
Monthly Notices of the Royal Astronomical Society, 467, 4872
 Vale A., Ostriker J. P., 2004, *MNRAS*, 353, 189
 Vogelsberger M., Genel S., Sijacki D., Torrey P., Springel V., Hernquist L.,
 2013, *Monthly Notices of the Royal Astronomical Society*, 436, 3031
 Vogelsberger M., Marinacci F., Torrey P., Puchwein E., 2020, *Nature Reviews
 Physics*, 2, 42
 Wang H., et al., 2018, *The Astrophysical Journal*, 852, 31
 Wang K., Mo H. J., Li C., Meng J., Chen Y., 2020, *Monthly Notices of the
 Royal Astronomical Society*, 499, 89
 Watson D. F., et al., 2015, *Monthly Notices of the Royal Astronomical Society*,
 446, 651
 Wechsler R. H., Tinker J. L., 2018, *Annual Review of Astronomy and Astro-
 physics*, 56, 435
 Weinberger R., et al., 2017, *Monthly Notices of the Royal Astronomical
 Society*, 465, 3291
 Wellons S., Torrey P., 2017, *Monthly Notices of the Royal Astronomical
 Society*, 467, 3887
 Wetzel A. R., Tinker J. L., Conroy C., 2012, *MNRAS*, 424, 232
 Wetzel A. R., Tinker J. L., Conroy C., van den Bosch F. C., 2013, *Monthly
 Notices of the Royal Astronomical Society*, 432, 336
 White S. D. M., Frenk C. S., 1991, *ApJ*, 379, 52
 White S. D. M., Rees M. J., 1978, *MNRAS*, 183, 341
 White M., Zheng Z., Brown M. J. I., Dey A., Jannuzi B. T., 2007, *ApJ*, 655,
 L69
 Yang X., Mo H. J., van den Bosch F. C., 2003, *Monthly Notices of the Royal
 Astronomical Society*, 339, 1057
 Yang X., Mo H. J., van den Bosch F. C., Pasquali A., Li C., Barden M., 2007,
The Astrophysical Journal, 671, 153
 Yang X., Mo H. J., van den Bosch F. C., 2009, *The Astrophysical Journal*,
 695, 900
 Yang X., Mo H. J., van den Bosch F. C., Zhang Y., Han J., 2012, *ApJ*, 752,
 41
 York D. G., et al., 2000, *AJ*, 120, 1579
 Zheng Z., Coil A. L., Zehavi I., 2007, *The Astrophysical Journal*, 667, 760
 van Dokkum P. G., et al., 2010, *The Astrophysical Journal*, 709, 1018
 van de Voort F., 2016, *Monthly Notices of the Royal Astronomical Society*,
 462, 778

APPENDIX A: SCATTER OF STELLAR MASS-HALO MASS RELATION IN TNG

The left panel of Fig. A1 shows the scatter of $\log(M_*/M_p)$ as function of redshift in bins of M_p from the TNG simulation. At each snapshot, we calculate the stellar mass to peak halo mass ratio for all galaxies and calculate the standard deviation in three peak halo mass bins, where the stellar mass and peak halo mass for TNG galaxies are defined in § 3.1. It can be seen that the scatter does not depend on redshift or M_p . The right panel of Fig. A1 shows the evolution of the Pearson correlation coefficient, i.e.

$$\rho(z) = \frac{\sum_i (r_{z,i} - \bar{r}_z)(r_{0,i} - \bar{r}_0)}{\sqrt{\sum_i (r_{z,i} - \bar{r}_z)^2 \times \sum_j (r_{0,j} - \bar{r}_0)^2}}, \quad (\text{A1})$$

where $r_{0,i} = \log(M_{*,0,i}/M_{d,0,i})$ is for galaxies at $z = 0$, $r_{z,i} = \log(M_{*,z,i}/M_{d,z,i})$ is for the main progenitor galaxies at the redshift of z . Here $M_{d,z,i}$ is the tentative stellar mass evaluated with the SHAM method (see equation (5)), and $M_{d,z,i}$ is the value at $z = 0$. We fit the evolution of the correlation coefficient for $M_{*,0} > 10^9 M_\odot$ with an exponential function, as shown by the red solid line and the annotation in the panel.

Fig. A2 shows the stellar mass evolution histories produced by applying our method to the TNG simulation with different choices of $\rho(z)$. As one can see, our results are insensitive to the specific choice of $\rho(z)$. From equations (2) and (5) one can see that both ϵ_0 and ϵ_z are random variables with means equal to zero. Thus, the effect of $\rho(z)$ is expected to be small as long as the sample of stellar mass histories is sufficiently large.

APPENDIX B: TEST PERFORMANCE ON EAGLE SIMULATION

To test the robustness of our method, we also apply our method to the EAGLE simulation (Schaye et al. 2015), which contains a series of cosmological simulations with state-of-the-art subgrid models with the GADGET-3 tree-SPH code (Springel et al. 2005). In this paper, we use the simulation with the identifier of Ref-L0100N1504, which was run with 2×1504^3 particles in a box with a side length of 100 comoving Mpc. The minimal mass for gas and stellar particles are $1.81 \times 10^6 M_\odot$ and $9.70 \times 10^6 M_\odot$, respectively. The simulation adopted a flat Λ CDM cosmology from the Planck mission (Collaboration et al. 2014) where $\Omega_m = 0.307$, $\Omega_\Lambda = 0.693$, $\Omega_b = 0.04825$, $\sigma_8 = 0.8288$, and $h = 0.6777$.

The peak halo mass and z_{starve} are defined in the same way as in the TNG simulation. The stellar mass we use is the sum of all stellar particles within 30 physical kpc, and the star formation rate is defined in the same aperture. We adopt the same $\rho(z)$ as given by equation (8) for consistency.

In Fig. B1, the solid lines show the normalized stellar mass functions of progenitors extracted from galaxy merger trees in the EAGLE simulation, and the results derived from our method using summary statistics of the EAGLE simulation are shown as dashed lines. Fig. B2 shows the median stellar mass evolution of main progenitor galaxies in the EAGLE simulation, where the results extracted from galaxy merger trees are shown by the shaded bands and the results obtained using our method are shown in symbols. One can see that our method can properly recover both the progenitor stellar mass distribution and the evolution of main progenitors.

This paper has been typeset from a \LaTeX file prepared by the author.

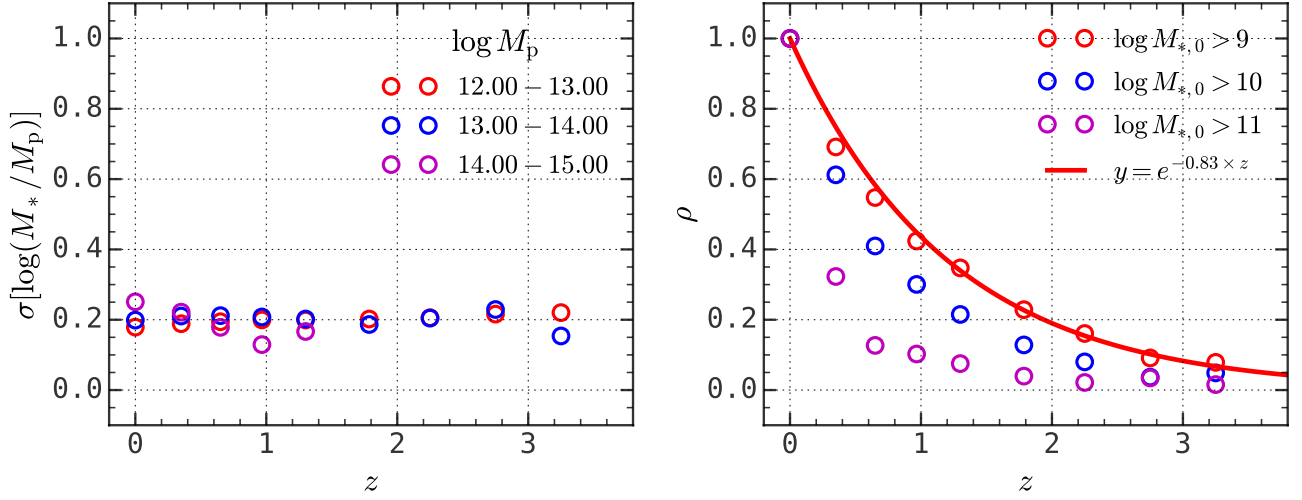


Figure A1. The left panel shows the scatter of the stellar mass-halo mass ratio, r , in TNG simulation from $z = 3$ to $z = 0$, in bins of peak halo mass at $z = 0$, M_p . The right panel shows the Pearson correlation coefficient defined in equation (A1), with the red solid curve showing the fitting result for $M_{*,0} > 10^9 M_\odot$.

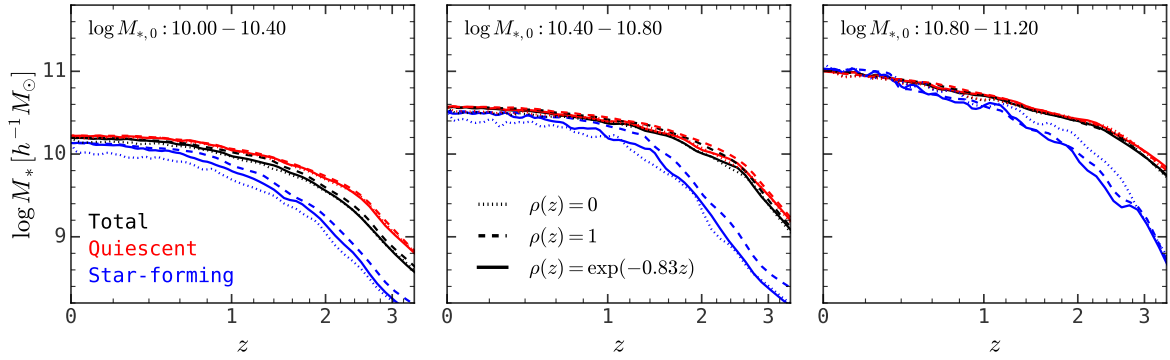


Figure A2. Median stellar mass evolution of main progenitor galaxies for descendant galaxies with $13 \leq \log M_0/[h^{-1} M_\odot] < 14$, predicted by applying our method to the TNG simulation. Dotted lines show results assuming $\rho(z) = 0$, i.e. the scatter of the $M_* - M_p$ relation is uncorrelated between adjacent snapshots. Dashed lines show results assuming $\rho(z) = 1$, i.e. the scatter of the $M_* - M_p$ relation is fully determined by the descendant mass at $z = 0$. The solid lines shows results with $\rho(z) = \exp(-0.83z)$, which is calibrated using the TNG simulation (see Fig. A1).

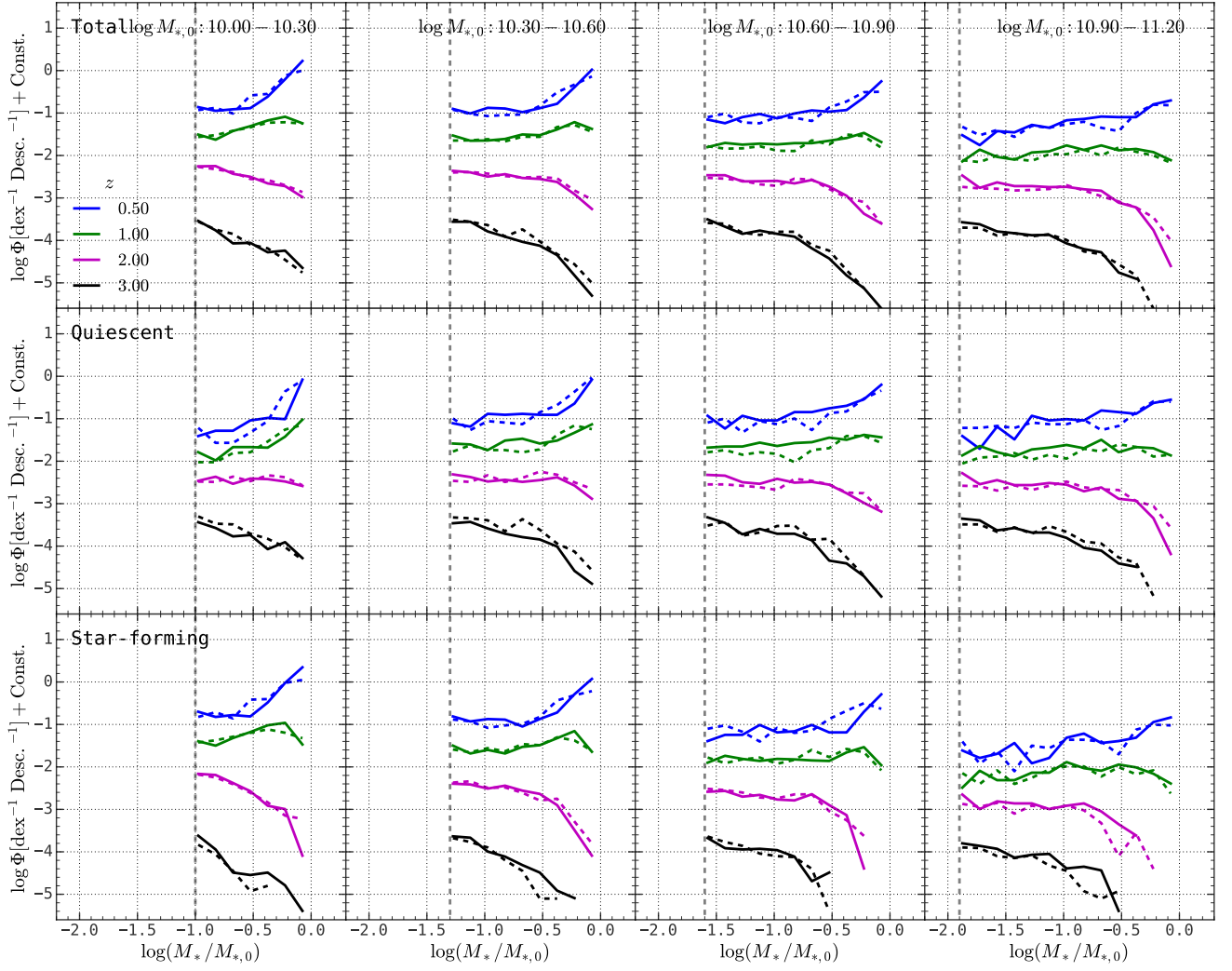


Figure B1. Similar to Fig. 2, but for the EAGLE simulation.

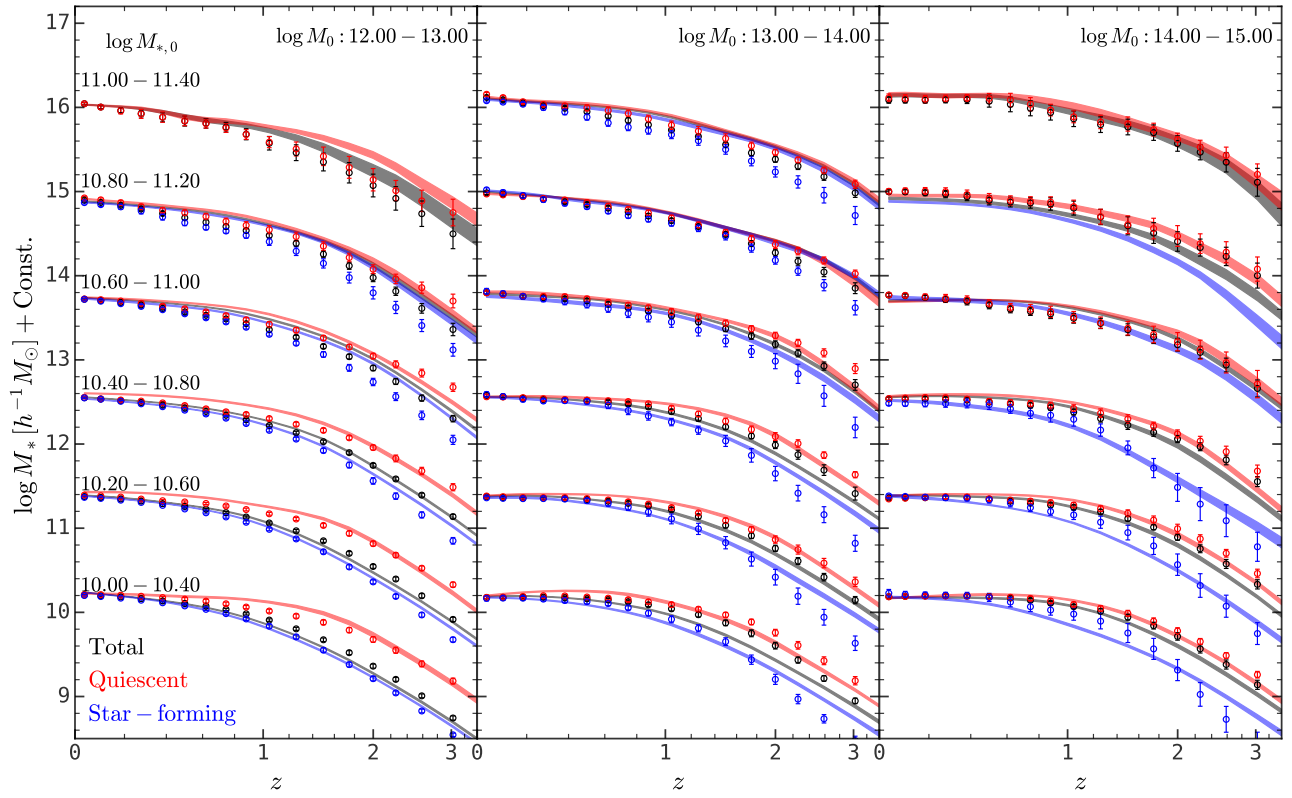


Figure B2. Similar to Fig. 3, just for the EAGLE simulation.